Dalton Transactions

ROYAL SOCIETY OF CHEMISTRY

PAPER

View Article Online
View Journal | View Issue

Cite this: *Dalton Trans.*, 2024, **53**, 12307

[Ag(IPr)(bpy)][PF_6]: brightness and darkness playing with aggregation induced phosphorescence for light-emitting electrochemical cells†

Ginevra Giobbio, [a,b] Pedro B. Coto, *[c] Jean-François Lohier,[a] Jean-Luc Renaud, [a,d] Sylvain Gaillard *[a] and Rubén D. Costa *[b]

Heteroleptic silver(I) complexes have recently started to attract attention in thin-film lighting technologies as an alternative to copper(I) analogues due to the lack of flattening distortion upon excitation. However, the interpretation of their photophysical behavior is challenging going from traditional fluorescence/phosphorescence to a temperature-dependent dual emission mechanism and ligand-lock assisted thermally activated delayed fluorescence. Herein, we unveil the photoluminescence behavior of a three-coordinated Ag(I) complex with the N-heterocyclic carbene (NHC) ligand and 2,2′-bipyridine (bpy) as the N^N ligand. In contrast to its low-emissive Cu(I) complex structural analogues, a strong greenish emission was attributed to the presence of aggregates formed by π–π intermolecular interactions as revealed by the X-ray structure and aggregation induced emission (AIE) studies in solution. In addition, the temperature-dependent time-resolved spectroscopic and computational studies demonstrated that the emission mechanism is related to a phosphorescence emission mechanism of two very close lying (ΔE = 0.08 eV) excited triplet states, exhibiting a similar delocalized nature over the bipyridine ligands. Unfortunately, this favourable AIE is lost upon forming homogeneous thin films suitable for lighting devices. Though the films showed very poor emission, the electrochemical stability under device operation conditions is remarkable compared to the prior-art, highlighting the potential of [Ag(NHC)(N^N)][X] complexes in thin-film lighting.

Received 10th April 2024,
Accepted 13th June 2024

DOI: 10.1039/d4dt01056f

rsc.li/dalton

Introduction

Known since ancient times, coinage metals have always played an important role in everyday life. Recently, modern chemistry fueled more sophisticated uses of d^{10}-metal derivatives. They have been widely exploited as catalysts,[1–8] while they have become more and more attractive for the replacement of rare and expensive metal-based active components, such as Ir(III), Ru(II) and Pt(II)-based compounds, in optoelectronics.[9–14]

In this context, the primacy of heteroleptic Cu(I)-complexes combining diimine (N^N) and diphosphine (P^P) ligands ([Cu(N^N)(P^P)]$^+$) for thin-films, solid-state lighting (*i.e.*, light-emitting electrochemical cells or LECs and organic light-emitting diodes or OLEDs)[15–17] and photovoltaics (*i.e.*, zombie dye-sensitized solar cells or DSSCs)[18,19] has been heralded owing to (i) their well-established chemistry to tune the photophysical and electrochemical properties and (ii) their highly efficient emission mechanism *via* thermally activated delayed fluorescence (TADF); the ability to harvest both singlet and triplet excitons leads to virtual lighting device efficiencies of 100%.[15,17,20,21] Conversely, the chemistry and the photophysical and electrochemical behaviors of their homologous Ag(I) complexes ([Ag(N^N)(P^P)]$^+$) have attracted much less attention.[12,22–33] However, research interest in silver(I) complexes is back with the promise to overcome the limitations of their copper(I) homologues arising from their labile coordination sphere.[24] In short, their emitting excited state features a strong metal-to-ligand charge transfer (MLCT) character, in which the metal ion center is formally oxidized (d^9 configuration), leading to a square-planar coordination geometry.[34] This flattening distortion causes (i) unforeseen changes in the

[a]*Normandy University, ENSICAEN, UNICAEN, CNRS, LCMT, 1400 Caen, France. E-mail: sylvain.gaillard@ensicaen.fr*
[b]*Technical University of Munich, Campus Straubing for Biotechnology and Sustainability, Chair of Biogenic Functional Materials, Schulgasse 22, 94315 Straubing, Germany. E-mail: ruben.costa@tum.de*
[c]*Spanish National Research Council (CSIC) and Donostia International Physics Center (DIPC), Material Physics Center (CFM), 20018 Donostia – San Sebastián, Spain. E-mail: pedro.brana@csic.es*
[d]*Sorbonne Université, CNRS, Institut Parisien de Chimie Moléculaire, UMR 8232, 75005 Paris, France*

†Electronic supplementary information (ESI) available. CCDC 2347259. For ESI and crystallographic data in CIF or other electronic format see DOI: https://doi.org/10.1039/d4dt01056f

emission features going from powder to solution and to thin films applied to devices,[35,36] (ii) a reduction of the photoluminescence quantum yield (ϕ),[17,37–39] and (iii) better accessibility of nucleophiles, like solvent molecules, forming non-emissive species during device fabrication.[40] In stark contrast, the 4d orbitals of the silver metal center are lower in energy compared to those related to the ligands. Thus, Ag(I) complexes are usually characterized by ligand-centered (LC) emitting excited states with a small MLCT contribution.[41] While this usually results in higher stabilities due to the lack of flattening distortion upon excitation,[24] the emission mechanism is difficult to predict even for similar heteroleptic [Ag(N^N)(P^P)]$^+$. Indeed, more and more contributions are disclosing complexes with standard emission mechanisms like fluorescence/phosphorescence[42,43] and others with, for example, more sophisticated temperature-dependent dual phosphorescence[44] and ligand-lock assisted TADF.[31,33] Finally, their application in OLEDs and LECs is also starting to flourish, highlighting limitations, such as formation of Ag(0) nanoclusters upon electrochemical stress.[22,28]

Herein, we expand the above prior-art designing of a three-coordinated Ag(I) complex bearing both an N-heterocyclic carbene (NHC) ligand and 2,2′-bipyridine (bpy) as the N^N ligand – Fig. 1. Previously, our copper(I) complex design proved to be effective for the stabilization of the metal center due to the strong σ-donation provided by the NHC ligand.[45–47] However, the rigidity of the bipyridyl ligand and the intermolecular π–π interactions led to low-emissive aggregates in powder form (λ_{em} = 639 nm, $\phi \geq 1\%$ – Fig. S1†).[45,48,49] In stark contrast, the same complex design for silver(I) complexes results in a highly emissive powder with a unique emission mechanism. In short, the intermolecular π–π interaction-induced aggregation phenomena activate a phosphorescence mechanism, leading to a remarkable ϕ value of 20% and a long excited state lifetime of around 571 μs. Joint temperature-dependent steady-state and time-resolved spectroscopy and theoretical studies confirmed the presence of two temperature equilibrated triplet excited states with experimental data rendering an energy splitting of 0.08 eV. Finally, this complex also exhibits a stable electrochemical behavior without showing the formation of Ag(0)-nanoclusters upon electrochemical stress. Thus, they were implemented into LECs that showed the expected ion-assisted electrical behavior with remarkable electrochemical stability, but no light response, since the lack of aggregation in the desired smooth and homogeneous active layers leads to the formation of non-emissive excitons. A trigonal Ag(I) complex with NHC and bipyridine ligands shows strong phosphorescence when aggregated into a powder. This aggregation-induced emission is lost in thin films, but the LEC devices show remarkable electrochemical stability.

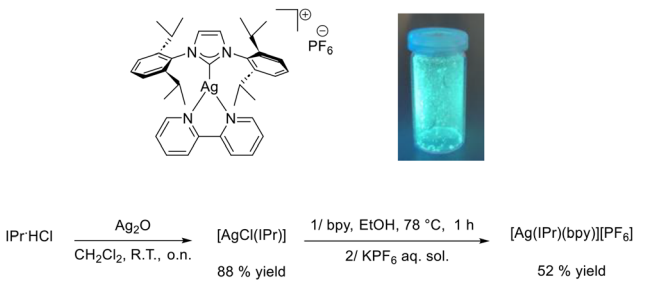

Fig. 1 The chemical structure, picture of the powder under 305 nm UV lamp irradiation, and synthesis scheme of [Ag(IPr)(bpy)][PF_6].

Results and discussion

Synthesis and structural characterization

At first, IPr (IPr = 1,3-bis(2,6-di-iso-propylphenyl)imidazol-2-ylidene) was selected as the NHC ligand for its well-known steric and σ-donation properties[50,51] and its wide use in copper congeners.[45–47] Then, following the procedure reported by Nolan and co-workers,[51] the [AgCl(IPr)] precursor was prepared in 88% isolated yield. The archetypal [Ag(IPr)(bpy)][PF_6] was synthesized using our previously reported procedure for analogous Cu(I) complexes.[45] In detail, a mixture of 1 eq. of [AgCl(IPr)] with 1.05 eq. of 2,2′-bipyridine (bpy) was heated up to 78 °C in EtOH for 1 h. Precipitation with a saturated aqueous solution of KPF_6 (10 eq.) furnished the expected complex. ^{1}H NMR analysis of the crude reaction showed the presence of 10% of the homoleptic complex [Ag(IPr)$_2$][PF_6]. However, two consecutive slow gas-diffusion recrystallizations, from a dichloromethane solution of the crude silver complex using diethyl ether as a light solvent, furnished the pure complex [Ag(IPr)(bpy)][PF_6] in 52% isolated yield as suggested by NMR spectroscopy. The coordination of the NHC ligand was confirmed by ^{13}C NMR spectroscopy in the presence of the typical two doublets centered at 186.2 ppm, resulting from the coupling between the carbenic carbon and the two magnetically active isotopes of silver (^{107}Ag and ^{109}Ag).[51]

Next, suitable single crystals were grown from a concentrated CH_2Cl_2 solution using a slow gas-diffusion technique with diethyl ether as a light solvent. X-ray diffraction analysis was conducted to unambiguously prove the structure. The most relevant values of bond lengths and angles are reported in Table 1 and Fig. 2, while all the structural values and experimental details are provided in the experimental part and in the ESI – Table S1.† In short, the 2,2′-bipyridine ligand and the Ag(I) metal centre formed the expected five-membered chelating ring. With the additional IPr ligand, the expected trigonal geometry for such a complex was also proven – Fig. 2.

Then, the Ag–C bond length was measured at 2.0723(12) Å and the two Ag–N bonds at 2.2928(11) and 2.2944(11) Å, in line with data from the literature.[51–53] The bite angle of the N^N ligands toward the metal center was found at 71.86(4)° which was smaller by around 10° than in the copper analogue reported previously (80.04(7)°).[45] The distances between the hydrogen atoms in the α position of the nitrogen atoms in 2,2′-bipyridine and the centroid of the N-substituted aromatic rings of NHC (CH···C_g) was estimated over 3 Å, resulting in the

Table 1 Selected bond lengths (Å) and angles (°) from the X-ray diffraction analysis of [Ag(IPr)(bpy)][PF_6]

Ag–C_{NHC} [Å]	Ag–N [Å]	N–Ag–N [°]	C_{NHC}–Ag–N [°]	CH···C_g [Å]	C_g···C_g distance [Å]	Displacement [°]
2.0723(12)	2.2928(11) 2.2944(11)	71.86(4)	142.31(4) 145.78(4)	3.09	3.82	21.26

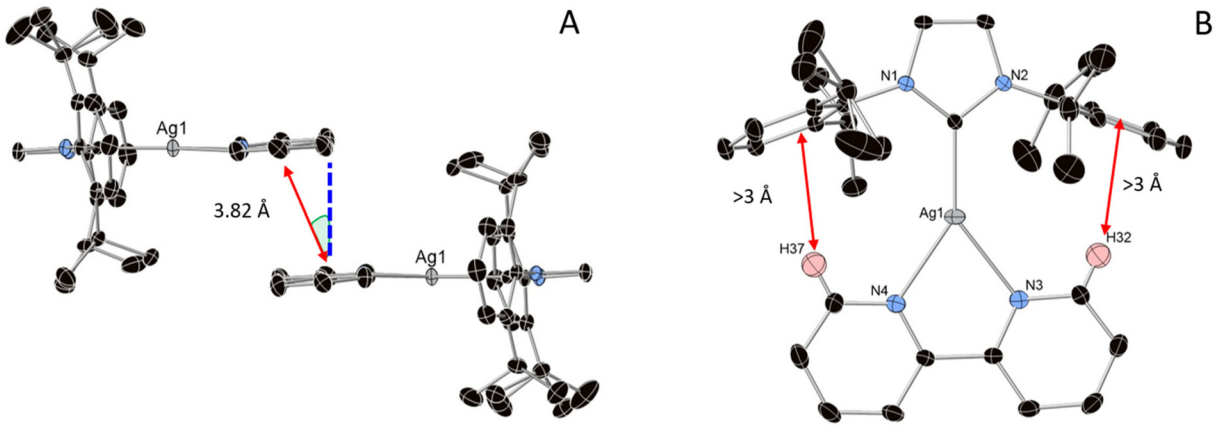

Fig. 2 (A) Ellipsoid representation at the 50% probability level from the X-ray diffraction analysis of [Ag(IPr)(bpy)][PF_6]: 2 molecules of [Ag(IPr)(bpy)][PF_6] in the crystal cells exhibiting π–π-interaction between bpy ligands. In the picture are graphically defined: the ring-centroid vector (red), the vector normal to the ring (blue), and the displacement angle (green). (B) One molecule of [Ag(IPr)(bpy)][PF_6] showing no CH–π interaction between bpy and IPr ligands. Anions and some hydrogen atoms are omitted for clarity.

loss of the CH–π interaction that was observed in the copper(I) complexes.[45] Nevertheless, long-range intermolecular π–π interactions occurred between the pyridines of the bpy ligand with a centroid–centroid (C_g···C_g) distance of 3.82 Å and displacement, defined as the angle between the centroid-ring vector and the ring normal, of 21.3° – Fig. 2.[54]

Photophysical and computational studies

The most relevant photophysical figures are summarized in Table 2. The UV-Vis absorption features in diluted solution (10^{-5} M in THF) show two typical structured bands centred at *ca.* 250 and 290 nm that are assigned to π–π* ligand-centred transitions – Fig. 3A, while a very weak (ϕ < 1%) and structured emission centred at 365 nm is associated with very short excited state lifetimes (τ) in the ns regime. Thus, this emission mechanism is attributed to a ligand-centered fluorescence. In stark contrast, the crystalline powder features a broad emission band centred at 500 nm – Fig. 3B, representing a significant wavelength shift of around 150 nm that is associated with ϕ and τ values of 18% and 571 μs, respectively. This could be attributed to a change of the nature of the excited state going from solution to crystalline powder form caused by the intermolecular π–π interactions described above. To investigate the presence of aggregation induced emission (AIE) phenomena,[55–57] we simply force the aggregation phenomena in THF solution (10^{-5} M) by adding different volume ratios of distilled water (f_w) – Fig. 3C. Upon increasing the f_w to 70% (v/v), a new low-energy emission band centred at 500 nm starts evolving, while a broad and intense emission similar to that of the crystalline powder was finally noted at f_w = 90%. Interestingly, the emission band shape as well as ϕ and τ values nicely match with those noted for powder – Table 2.

Table 2 Photophysical properties of [Ag(IPr)(bpy)][PF_6] in powder, solution, and thin films

Conditions [a]	Parameters	Data
THF solution	λ_{abs} (ε)/nm (10^4 L mol^{-1} cm^{-1})	258 (1.45), 296 (1.17), 318 (1.32)
	λ_{em} 298 K nm^{-1}	321, 365
	τ 298 K ns^{-1}	11.3
	ϕ/%	<1
Powder	λ_{em} 298 K nm^{-1}	498
	λ_{em} 77 K nm^{-1}	428
	τ 298 K μs^{-1}	571
	τ 77 K ms^{-1}	13.8
	ϕ/%	20
90 : 10 v% H_2O/THF solution	λ_{em} 298 K nm^{-1}	502
	τ 298 K ms^{-1}	464
	ϕ/%	18
Spin coated thin film	λ_{em} 298 K nm^{-1}	540
	τ 298 K μs^{-1}	133
	ϕ/%	2
Dropcast thin film	λ_{em} 298 K nm^{-1}	497
	τ 298 K ms^{-1}	449
	ϕ/%	18

[a] λ_{ex} = 290 nm for emission (λ_{em}), lifetime (τ) and quantum yield (ϕ).

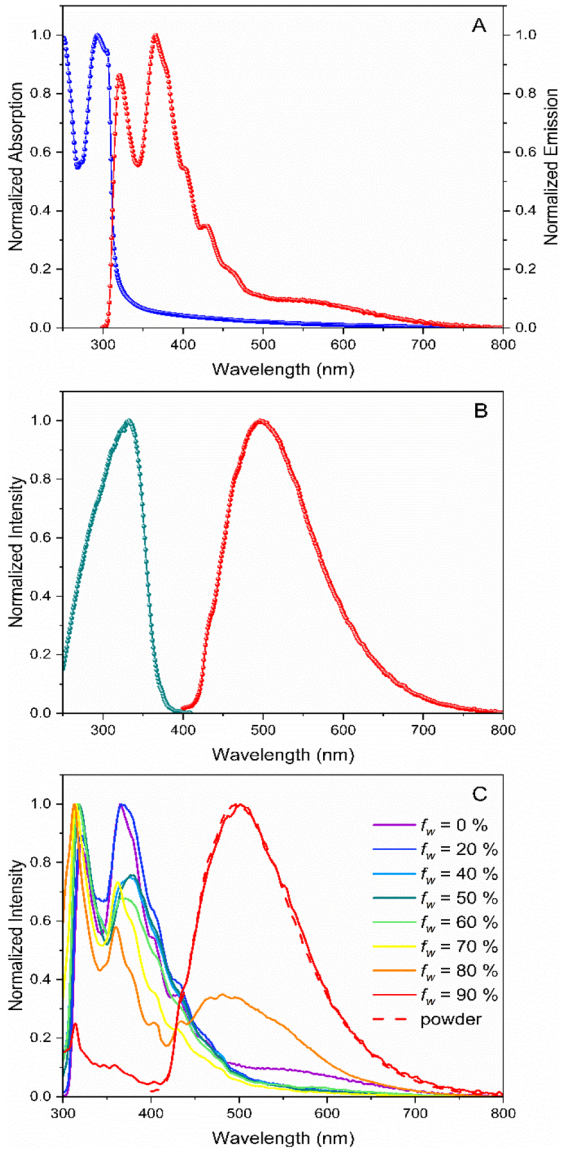

Fig. 3 (A) UV-Vis absorption (blue) and emission (red) spectra of [Ag(IPr)(bpy)][PF_6] in THF solution. (B) Emission (red) and excitation (green) spectra of [Ag(IPr)(bpy)][PF_6] in powder at RT. (C) Emission spectral changes of [Ag(IPr)(bpy)][PF_6] in volume mixtures of THF : H_2O – see the legend, highlighting the AIE effect that leads to the same emission band in any aggregated state (powder and solution suspension).

The τ values of [Ag(IPr)(bpy)][PF_6] are around 500 μs, suggesting that the AIE phenomenon induces a change in the emission mechanism from fluorescence (THF solution) to phosphorescence (aggregated state in solution and powder).

To further study the emission mechanism, temperature-dependent emission was carried for the powder samples going from 77 K to 400 K – Fig. 4. Here, the emission band is red-shifted from 458 nm at 77 K to 498 nm at 300 K, indicating that this complex does not feature the typical TADF mechanism (*i.e.* a blue-shifted emission at 298 K related to the lowest emitting triplet excited state in thermal equilibrium with its singlet excited state), but a temperature-dependent dual-phosphorescence mechanism – Fig. 4A. This is confirmed by the τ *vs.* T plot that follows a Boltzmann-type distribution described using eqn (1) – Fig. 4B:[44]

$$\tau_{em}(T) = \frac{1 + \exp\left(\frac{-\Delta E(T_{1A} - T_{1B})}{k_B T}\right)}{\frac{1}{\tau(T_{1B})} + \frac{1}{\tau(T_{1A})}\exp\left(\frac{-\Delta E(T_{1A} - T_{1B})}{k_B T}\right)} \quad (1)$$

where k_B is the Boltzmann constant, $\Delta E(T_{1A}–T_{1B})$ is the energy gap between the two excited states and $\tau(T_{1A})$ and $\tau(T_{1B})$ are the excited state decay lifetimes of the respective triplet excited states. This fitting indicates the presence of a temperature-equilibrated dual phosphorescence mechanism from two triplet excited states, namely T_{1A} and T_{1B}, with triplet–triplet energy splitting of $\Delta E(T_{1A}–T_{1B})$ = 0.08 eV. To get more insights into the nature of these triplet excited states, they were modelled using density functional theory (DFT) and its time-dependent version (TD-DFT) methodology – see the experimental section; Tables S2–S4 and Fig. S6.† This confirmed the presence of two low-lying triplet equilibrium structures where the triplet states are delocalized over the two bipyridine ligands – see the ESI.† In line with the experimental data, these states exhibit a very small energy difference (adiabatic $\Delta E(T_{1A}–T_{1B})$ = 0.008 eV), while the calculated singlet excited states might not thermally accessible with a singlet–triplet energy gap of *ca.* 0.88 eV, suggesting the possible lack of TADF mechanism. Finally, vertical energy differences ($T_{1A/B} \rightarrow S_0$) of 2.60 eV (477 nm) and 2.58 eV (481 nm) were found for T_{1A} and T_{1B}, respectively – Tables S2–4,† supporting the assignment of the emission mechanism. Though the presence of thermally stimulated and equilibrated phosphorescence processes in related Ag(I) complexes has been recently discussed,[44] this is the first example of aggregation induced dual phosphorescence in this type of emitter.

Finally, we also studied the photoluminescence features in thin films similar to those applied in devices – *vide infra*. The films were prepared *via* spin-coating deposition onto a quartz slide from 15 mg ml^{-1} acetonitrile solutions, forming homogeneous films with no visual aggregates and a roughness below 1 nm – Fig. 5A. In contrast to the photoluminescence in solution and powder, the emission of the films consists of a broad band centered at 540 nm (*i.e.*, 40 nm red-shifted) and exhibits a dramatic reduction of the ϕ and τ values (*i.e.*, <2.0% and 133 μs; Table 2 and Fig. 5A). This is typically ascribed to aggregation induced quenching phenomena occurring upon film formation.[36] Here, the formation of aggregates induced by the quick drying of the solvent upon spinning as well as the presence of solvent molecules leads to a non-emissive species, in which short- and long-range intermolecular interactions are different from those noted in their X-ray structures. Indeed, drop-cast films formed by slow evaporation under ambient conditions led to non-homogeneous films with the same photoluminescence features similar to those in powder – Table 2 and Fig. 5B. Though aggregation is key to unlocking the photoluminescence features of [Ag(IPr)(bpy)][PF_6], our

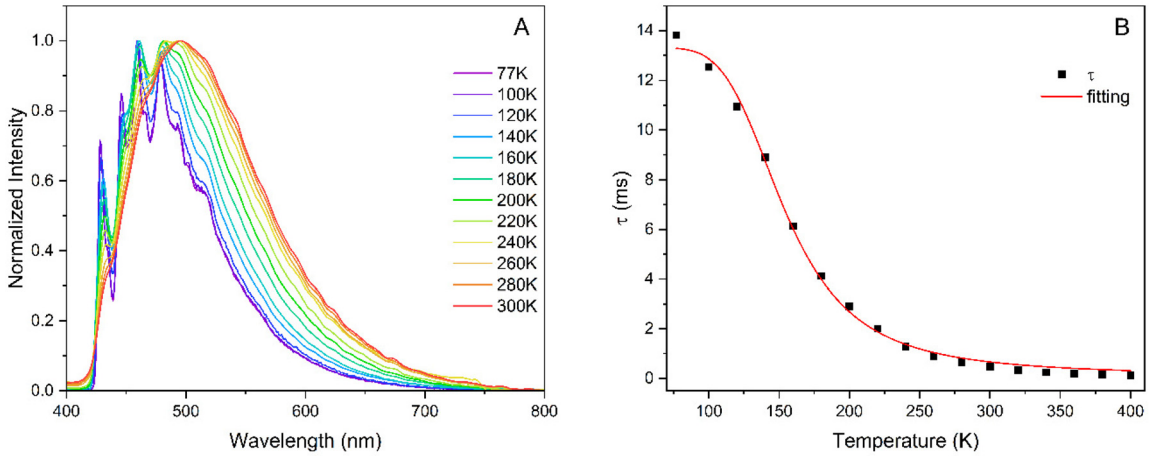

Fig. 4 (A) Emission spectra of [Ag(IPr)(bpy)][PF_6] in powder at different temperatures – see the legend. (B) τ *vs.* *T* plot along the fitted eqn (1) (red).

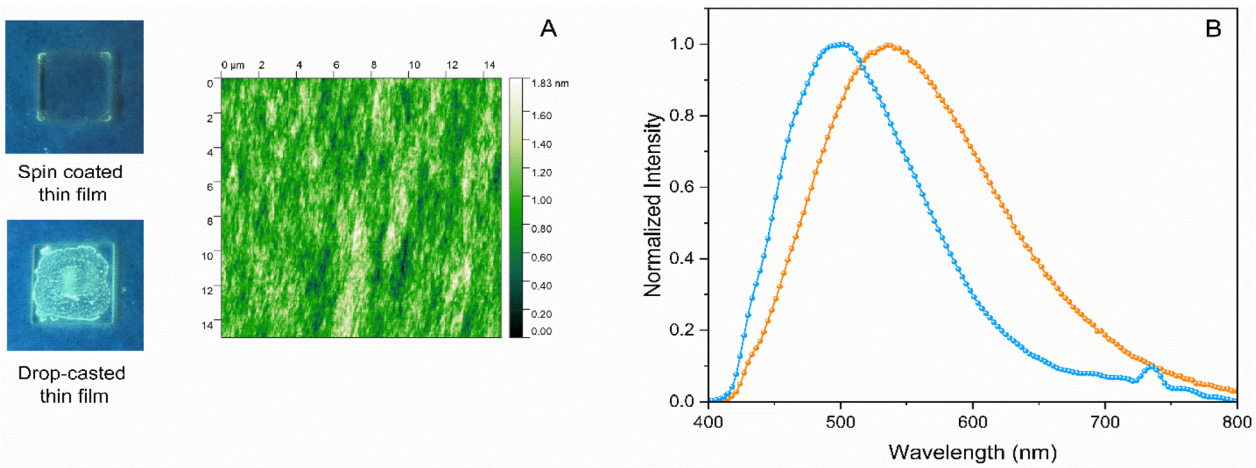

Fig. 5 (A) Picture of spin-coated and drop-cast films under UV-lamp irradiation and the atomic force microscopy (AFM) picture to highlight the homogeneous morphology of the spin-coated thin films. (B) Emission spectra of [Ag(IPr)(bpy)][PF_6] in thin-films prepared *via* spin-coating (orange) and drop-casting (azure).

efforts changing thin-film forming conditions (spinning/blading, solvents, and additives, such as ionic liquids and polymers) did not lead to simultaneously meeting good film quality for devices and photoluminescence features similar to those in powder.

Preparation and characterization of LECs

Despite the poor photoluminescence features in thin films, we decided to study the electroluminescence behavior in LECs. In short, a layer (70 nm) of poly(3,4-ethylene dioxythiophene): polystyrene sulfonate (PEDOT:PSS) was spin-coated onto a clean indium-tin-oxide (ITO) electrode-coated glass to increase reproducibility. Then, the active layer (*ca.* 90 nm) was deposited *via* spin-coating as explained above. Finally, 100 nm of the aluminum cathode was deposited *via* physical vapour deposition to finalize the devices' architecture. The devices were driven at a pulsed current of 8 mA, using a 1 kHz block-wave and 50% duty cycle on 10 mm^2 pixels. Unfortunately, all the devices did not light up as expected by the poor photophysical features in thin films, but showed a stable electrical behavior compared to that of the prior-art – Fig. 6A.[22,28,44] In detail, the average voltage reduces exponentially until a stable plateau is reached. This is related to the formation of electrical double layers (EDLs) at the electrode interface by the drifting of ions upon applying an external electric field. The second stage is achieved once the ohmic contacts are formed. Here, charge injection is stable and the doped regions are slowly growing until a stable p-*i*-n junction is formed. This is typically affected by the electrochemical degradation of the oxidized/reduced species that leads to unforeseen changes in the average voltage profile over time that either increase caused by the formation of carrier trappers, (*e.g.*, Cu(II) species in the case of Cu(I)-based devices)[58] or decrease caused by the formation of highly conductive degradative compounds, such as

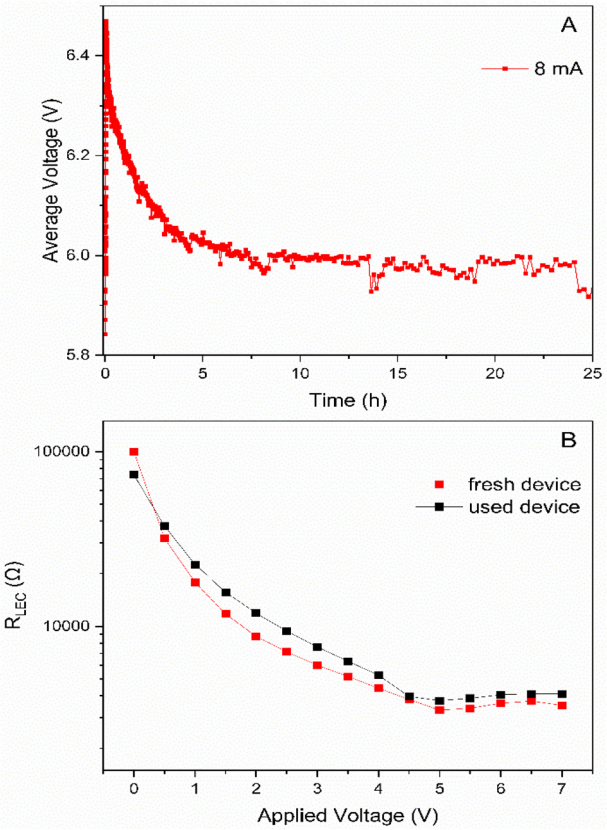

Fig. 6 (A) Average voltage profile *vs.* time of [Ag(IPr)(bpy)][PF_6]-based LECs operating at a pulsed current of 8 mA. (B) LEC resistance *vs.* applied voltage for fresh and used [Ag(IPr)(bpy)][PF_6] based LECs – see the legend.

Ag(0) nanoclusters.[28] Since the voltage profile is stable, we can infer that electrochemical degradation of [Ag(IPr)(bpy)][PF_6] in thin-films is not happening. Electrochemical impedance spectroscopy (EIS) assays were performed to further investigate the electrical behavior using a single resistor/capacitor equivalent circuit to analyse the dominant processes upon increasing the applied voltage – Fig. S7.†[59] Thus, the device resistance profile is characterized by (i) an exponential decrease during the formation of the EDLs at low applied voltages before carrier injection occurs and (ii) a linear regime related to a balanced growth of the p- and n-regions at voltages above the electrochemical band-gap of the complex.[60–62] The representative values calculated at 0 V are dielectric constant (ε_r) and ionic conductivity (σ) that are 13.95 and 8.08 × 10^{-8} S m^{-1}, respectively. While the ε_r value is high compared to that of other thin-films with similar d^{10}-complexes,[60–62] suggesting that the formation of EDLs is highly favourable in [Ag(IPr)(bpy)][PF_6], and the σ values are two-order of magnitude lower, indicating that the growing of the doped regions must be slower than in analogues complexes. However, the most relevant feature is the lack of meaningful changes in the resistance profile of the device upon comparing both fresh and used devices – Fig. 6. This nicely confirms that the electrochemical stability of [Ag(IPr)(bpy)][PF_6] thin-films is remarkable.

Conclusions

This work highlights the bright and dark sides of unique aggregation induced emission (AIE) in archetypal tri-coordinate [Ag(IPr)(bpy)][PF_6] complexes. Intermolecular π–π interactions determined in the X-ray structures play a pivotal role in the photophysical behavior of the complex that shows a remarkable ϕ value of 20%. What is more, temperature-dependent lifetime measurement revealed the presence of a phosphorescence behavior related to two thermally interconnected triplet excited states (ΔE of 0.08 eV). This was further supported by computational studies that determined the presence of two very close lying excited triplet states (adiabatic ΔE of 0.008 eV) with a similar delocalized nature over the bipyridine ligands. Unfortunately, this favorable AIE is lost upon forming homogeneous thin-films suitable for lighting devices. Here, films feature very poor emission with ϕ < 2% which leads to dark LECs. However, the electrical behavior of the device is outstanding compared to that of devices with tetragonal heteroleptic Ag(I) complexes, since the formation of Ag(0) nanoclusters is not observed by electrochemical impedance spectroscopy. Finally, the photophysical characteristics and the stability of [Ag(IPr)(bpy)][PF_6] open up new possibilities for the exploration of new [Ag(NHC)(N^N)][X] complexes, seeking the optimization of the AIE behavior upon device fabrication.

Experimental part

General considerations

Synthesis. All the commercially available compounds were purchased and used without further purification. All the reactions were performed under a dry argon atmosphere, using standard Schlenk techniques. The purchased solvents were degassed by bubbling Ar directly in bulk. Details about the synthesis and the characterization of [Ag(IPr)(bpy)][PF_6] are provided in the ESI.†

Crystallography. Crystallographic data sets were collected from single-crystal samples, performing the analysis with a Brüker Kappa APEXII CCD diffractometer. The initial unit cell parameters were determined by a least-squares fit of the angular setting of strong reflections, collected by a 6.0° scan in 12 frames over three different parts of the reciprocal space (36 frames total). Cell refinement and data reduction were performed with SAINT (Brüker AXS). Absorption correction was done by a multiscan method using SADABS 2012/1 (Brüker AXS). The structure was solved by direct methods and refined using SHELXL-97 or SHELXL-2013 (Sheldrick). All non-H atoms were refined by full-matrix least-squares with anisotropic displacement parameters while hydrogen atoms were placed in idealized positions. The short interactions were calculated using the software Platon version 250420.

Photophysical measurements. UV-Vis absorption spectra in solution were recorded at room temperature with a Shimadzu UV/2600i spectrometer. Steady-state emission spectra and ϕ were measured with an FS5 spectrofluorometer (Edinburgh

Instruments) equipped with an integrating sphere. The measurements of time-resolved photoluminescence were performed using Multi-Channel Scaling (MCS) as the photocounting method and a pulsed μs Xe-flash lamp as the excitation source (Edinburgh Instruments, FS5 spectrofluorometer). For temperature-dependent measurements, the FS5 spectrofluorometer (SC-80 holder) was equipped with an optical cryostat (Optistat-DN, Oxford Instruments). The intensity-weighted intensity lifetime was used in the case of biexponential decays of the excited state.[63] Thin-films for optical characterization were prepared by spin-coating the complex filtered solution (15 mg ml^{-1} in acetonitrile, thickness: 90 nm) onto clean quartz slides. AFM of the resulting samples was performed with MFP-3D Origin + Oxford Instruments to confirm the suitable morphology of the layers.

Theoretical details. The relaxed structures of the lowest-lying triplet states were obtained using a [Ag(IPr)(bpy)][PF_6] dimer obtained from the X-ray resolved structure. Geometry relaxation was carried out using linear response time-dependent density functional theory (TDDFT)[64] employing the CAM-B3LYP exchange-correlation potential[65] and the def2-TZVP basis set.[66] Dispersion interactions were accounted for using the dispersion correction of Grimme and co-workers including the Becke–Johnson damping.[67,68] The core electrons of Ag were described using the def2-ECP pseudopotential.[69] The structural relaxations were carried out enforcing C_i symmetry (T_{1A} (^{3}Au) and T_{1B} (^{3}Ag)) and imposing geometrical constraints to keep the relative orientation found in the crystal structure (see the ESI†). The characterization of the triplet excited states was carried out using density difference plots. All these calculations were carried out using Turbomole 7.6.[70,71] Spin–orbit coupling TDDFT calculations including 20 singlet and 20 triplet states were carried out at the relaxed structures using the zero-order regular approximation (ZORA) Hamiltonian,[72,73] the CAM-B3LYP exchange–correlation functional, and the ZORA recontracted def2-TZVP and SARC-ZORA-TZVP basis set for Ag[74] as implemented in ORCA 5.0.3.[75,76] The corresponding Coulomb fitting auxiliary basis sets were used.[77,78] The spin–orbit integrals were calculated using the RI-SOMF(1X) approximation.[79]

Device preparation and characterization. Narajo Substrates provided ITO (130 nm) substrates. The substrate is cleaned in four steps with water diluted Derquim® detergent (ratio 1 : 1), distilled water, ethanol and propan-2-ol as solvents in a warm ultrasonic bath (60 °C, 37–70 Hz) for 15 min at each step. Then, the substrates were dried in N_2 flow and treated in a UV-ozone cleaner for 8 min. The aqueous PEDOT:PSS (Clevios P VP.Al4083) was diluted with propan-2-ol (ratio 3 : 1). The resulting solution was sonicated at room temperature for 15 min and then filtered (0.45 μm pore diameter) before the spin-coating onto the clean ITO substrates. The resulting layers were dried on a heating plate at 120 °C and stored in a glovebox (N_2 atmosphere, <0.1 ppm O_2 and H_2O, Ångstrom Engineering). The complex was dissolved in acetonitrile, reaching a concentration of 15 mg ml^{-1}. The solution was sonicated for 10 min and filtered before the deposition. The films were prepared by spin-coating of 60 μl of solution with a three-step deposition program (800 rpm, 30 s; 1500 rpm, 30 s; and 3000 rpm, 10 s) reaching thick layers (95 nm). Then, the active layers were dried in a vacuum overnight. Finally, the aluminum cathode was deposited onto the active layer *via* physical vapor deposition (Ångstrom Covap evaporator integrated with the glovebox, $<1 \times 10^{-6}$ mbar). A shadow mask was used to define pixels with an area of 10 mm^2. Voltage and current performances of the devices were evaluated with a Botest OLT OLED Lifetime-Test System operating in the pulsed mode. A Metrohm μAutolab III potentiostat/galvanostat equipped with a frequency analyzer module (FRA2) was used to carry out electrochemical spectroscopy (ESI) assays. The range of the applied voltage was set between 0 V and 7 V and fitted (Nova 2.1) with the equivalent circuit model reported in the ESI – S18.†

Conflicts of interest

There are no conflicts to declare.

Acknowledgements

This work was supported by the "Ministère de l'Enseignement Supérieur et de la Recherche", CNRS (Centre National de la Recherche Scientifique) and the LABEX SynOrg (ANR-11-LABX-0029). S. G. acknowledges the "Région Normandie" (G. G.), the Graduate School of Research XL-Chem (ANR-18-EURE-0020 XL-Chem) for funding.

References

1 S. Saranya and G. Anilkumar, *Copper Catalysis in Organic Synthesis*, John Wiley & Sons, Ltd, 2020, pp. 1–5.
2 A. S. K. Hashmi, *Chem. Rev.*, 2007, **107**, 3180.
3 A. S. K. Hashmi and G. J. Hutchings, *Angew. Chem., Int. Ed.*, 2006, **45**, 7896.
4 S. A. Shahzad, M. A. Sajid, Z. A. Khan and D. Canseco-Gonzalez, *Synth. Commun.*, 2017, **47**, 735.
5 S. Witzel, A. S. K. Hashmi and J. Xie, *Chem. Rev.*, 2021, **121**, 8868.
6 A. M. Echavarren, N. Jiao and V. Gevorgyan, *Chem. Soc. Rev.*, 2016, **45**, 4445.
7 Q.-Z. Zheng and N. Jiao, *Chem. Soc. Rev.*, 2016, **45**, 4590.
8 K. Sekine and T. Yamada, *Chem. Soc. Rev.*, 2016, **45**, 4524.
9 A. Barbieri, G. Accorsi and N. Armaroli, *Chem. Commun.*, 2008, 2185.
10 J. Feng, A.-P. M. Reponen, A. S. Romanov, M. Linnolahti, M. Bochmann, N. C. Greenham, T. Penfold and D. Credgington, *Adv. Funct. Mater.*, 2021, **31**, 2005438.
11 J. Hossain, R. Akhtar and S. Khan, *Polyhedron*, 2021, **201**, 115151.

12 C.-W. Hsu, C.-C. Lin, M.-W. Chung, Y. Chi, G.-H. Lee, P.-T. Chou, C.-H. Chang and P.-Y. Chen, *J. Am. Chem. Soc.*, 2011, **133**, 12085.
13 M. Osawa, I. Kawata, R. Ishii, S. Igawa, M. Hashimoto and M. Hoshino, *J. Mater. Chem. C*, 2013, **1**, 4375.
14 T. S. Teets, D. V. Partyka, A. J. Esswein, J. B. Updegraff, M. Zeller, A. D. Hunter and T. G. Gray, *Inorg. Chem.*, 2007, **46**, 6218.
15 G. U. Mahoro, J. Fernandez-Cestau, J.-L. Renaud, P. B. Coto, R. D. Costa and S. Gaillard, *Adv. Opt. Mater.*, 2020, **8**, 2000260.
16 E. Fresta and R. D. Costa, *J. Mater. Chem. C*, 2017, **5**, 5643.
17 R. Czerwieniec, M. J. Leits, H. H. H. Homeier and H. Yersin, *Coord. Chem. Rev.*, 2016, **325**, 2.
18 M. Freitag, Q. Daniel, M. Pazoki, K. Sveinbjörnsson, J. Zhang, L. Sun, A. Hagfeldt and G. Boschloo, *Energy Environ. Sci.*, 2015, **8**, 2634.
19 Y. Saygili, M. Stojanovic, H.-S. Kim, J. Teuscher, R. Scopelliti, M. Freitag, S. M. Zakeeruddin, J.-E. Moser, M. Grätzel and A. Hagfeldt, *J. Phys. Chem. C*, 2020, **124**, 7071.
20 C. E. Housecroft and E. C. Constable, *J. Mater. Chem. C*, 2022, **10**, 4456–4482.
21 N. Armaroli and H. J. Bolink, *Top. Curr. Chem.*, 2016, **374**, 44.
22 O. Moudam, A. C. Tsipis, S. Kommanaboyina, P. N. Horton and S. J. Coles, *RSC Adv.*, 2015, **5**, 95047.
23 A. Kaeser, O. Moudam, G. Accorsi, I. Séguy, J. Navarro, A. Bel-bakra, C. Duhayon, N. Armaroli, B. Delavaux-Nicot and J.-F. Nieren-garten, *Eur. J. Inorg. Chem.*, 2014, **8**, 1345.
24 M. Z. Shafikov, A. F. Suleymanova, R. Czerwieniec and H. Yersin, *Chem. Mater.*, 2017, **29**, 1708.
25 M. Z. Shafikov, A. F. Suleymanova, A. Schinabeck and H. Yersin, *J. Phys. Chem.*, 2018, **9**, 702.
26 D. Zare, C. Piguet, A. Prescimone, C. E. Housecroft and E. C. Constable, *Chem. – Eur. J.*, 2022, **28**, e202200912.
27 J. M. Carbonell-Vilar, E. Fresta, D. Armentano, R. D. Costa, M. Viciano-Chumillas and J. Cano, *Dalton Trans.*, 2019, **48**, 9765.
28 E. Fresta, J. M. Carbonell-Vilar, J. Yu, D. Armentano, J. Cano, M. Viciano-Chumillas and R. D. Costa, *Adv. Funct. Mater.*, 2019, **29**, 1901797.
29 A. V. Artem'ev, M. Z. Shafikov, A. Schinabeck, O. V. Antonova, A. S. Berezin, I. Y. Bagryanskaya, P. E. Plusnin and H. Yersin, *Inorg. Chem. Front.*, 2019, **6**, 3168.
30 M. Z. Shafikov, R. Czerwieniec and H. Yersin, *Dalton Trans.*, 2019, **48**, 2802.
31 T. Teng, K. Li, G. Cheng, Y. Wang, J. Wang, J. Li, C. Zhou, H. Liu, T. Zou, J. Xiong, C. Wu, H.-X. Zhang, C.-M. Che and C. Yang, *Inorg. Chem.*, 2020, **59**, 12122.
32 M. Calvo, O. Crespo, M. C. Gimeno, A. Laguna, M. T. Oliván, V. Polo, D. Rodríguez and J.-M. Sáez-Rocher, *Inorg. Chem.*, 2020, **59**, 14447.
33 J.-H. Jia, D. Liang, R. Yu, X.-L. Chen, L. Meng, J.-F. Chang, J.-Z. Liao, M. Yang, X.-N. Li and C.-Z. Lu, *Chem. Mater.*, 2020, **32**, 620.
34 C. Förster and K. Heinze, *Chem. Soc. Rev.*, 2020, **49**, 1057.
35 E. Fresta, G. U. Mahoro, L. M. Cavinato, J.-F. Lohier, J.-L. Renaud, S. Gaillard and R. D. Costa, *Adv. Opt. Mater.*, 2022, **10**, 2101999.
36 E. Fresta, G. Volpi, C. Garino, C. Barolo and R. D. Costa, *Polyhedron*, 2018, **140**, 129.
37 M. Iwamura, S. Takeuchi and T. Tahara, *Acc. Chem. Res.*, 2015, **48**, 782.
38 M. W. Mara, K. A. Fransted and L. X. Chen, *Coord. Chem. Rev.*, 2015, **282–283**, 2.
39 H. Yersin, R. Czerwieniec, M. Z. Shafikov and A. F. Suleymanova, *ChemPhysChem*, 2017, **18**, 3508.
40 C. T. Cunningham, J. J. Moore, K. L. H. Cunningham, P. E. Fanwick and D. R. McMillin, *Inorg. Chem.*, 2000, **39**, 3638.
41 M. Z. Shafikov, A. F. Suleymanova, R. Czerwieniec and H. Yersin, *Inorg. Chem.*, 2017, **56**, 13274.
42 M. Barwiolek, A. Wojtczak, A. Kozakiewicz, R. Szczesny, M. Babinska, L. Skowronski and E. Szlyk, *New J. Chem.*, 2018, **42**, 18559.
43 A. Castiñeiras and R. Pedrido, *Inorg. Chem.*, 2009, **48**, 4847.
44 S. Lipinski, L. M. Cavinato, T. Pickl, G. Biffi, A. Pöthig, P. B. Coto, J. Fernández-Cestau and R. D. Costa, *Adv. Opt. Mater.*, 2023, **11**, 2203145.
45 R. Marion, F. Sguerra, F. Di Meo, E. Sauvageot, J.-F. Lohier, R. Daniellou, J.-L. Renaud, M. Linares, M. Hamel and S. Gaillard, *Inorg. Chem.*, 2014, **53**, 9181.
46 M. Elie, F. Sguerra, F. Di Meo, M. D. Weber, R. Marion, A. Grimault, J.-F. Lohier, A. Stallivieri, A. Brosseau, R. B. Pansu, J.-L. Renaud, M. Linares, M. Hamel, R. D. Costa and S. Gaillard, *ACS Appl. Mater. Interfaces*, 2016, **8**, 14678.
47 M. Elie, M. D. Weber, F. Di Meo, F. Sguerra, J.-F. Lohier, R. B. Pansu, J.-L. Renaud, M. Hamel, M. Linares, R. D. Costa and S. Gaillard, *Chem. – Eur. J.*, 2017, **23**, 16328.
48 V. A. Krylova, P. I. Djurovich, M. T. Whited and M. E. Thompson, *Chem. Commun.*, 2010, **46**, 6696.
49 K. A. Barakat, T. R. Cundari and M. A. Omary, *J. Am. Chem. Soc.*, 2003, **125**, 14228.
50 D. Bourissou, O. Guerret, F. P. Gabbaï and G. Bertrand, *Chem. Rev.*, 2000, **100**, 39–92.
51 P. de Frémont, N. M. Scott, E. D. Stevens, T. Ramnial, O. C. Lightbody, C. L. B. Macdonald, J. A. C. Clyburne, C. D. Abernethy and S. P. Nolan, *Organometallics*, 2005, **24**, 6301.
52 S. D. Adhikary, A. Mondal, H. K. Kisan, C. W. Bielawski and J. Dinda, *Appl. Organomet. Chem.*, 2020, **34**, e5335.
53 L. Jhiulki, R. Purkait, H. K. Kisan, V. Bertolasi, A. A. Isab, C. Sinha and J. Dinda, *Appl. Organomet. Chem.*, 2020, **34**, e5663.
54 C. Janiak, *J. Chem. Soc., Dalton Trans.*, 2000, 3885.
55 J. Luo, Z. Xie, J. W. Y. Lam, L. Cheng, B. Z. Tang, H. Chen, C. Qiu, H. S. Kwok, X. Zhan, Y. Liu and D. Zhu, *Chem. Commun.*, 2001, 1740–1741.
56 Y. Hong, J. W. Y. Lam and B. Z. Tang, *Chem. Commun.*, 2009, 4332.
57 J. Mei, N. L. C. Leung, R. T. K. Kwok, J. W. Y. Lam and B. Z. Tang, *Chem. Rev.*, 2015, **115**, 11718.

58 M. D. Weber, E. Fresta, M. Elie, M. E. Miehlich, J.-L. Renaud, K. Meyer, S. Gaillard and R. D. Costa, *Adv. Funct. Mater.*, 2018, **28**, 1707423.
59 S. B. Meier, D. Hartmann, A. Winnacker and W. Sarfert, *J. Appl. Phys.*, 2014, **116**, 104504.
60 B. M. D. Puscher, M. F. Aygüler, P. Docampo and R. D. Costa, *Adv. Energy Mater.*, 2017, **7**, 1602283.
61 M. D. Weber, M. Viciano-Chumillas, D. Armentano, J. Cano and R. D. Costa, *Dalton Trans.*, 2017, **46**, 6312.
62 E. Fresta, M. D. Weber, J. Fernandez-Cestau and R. D. Costa, *Adv. Opt. Mater.*, 2019, **7**, 1900830.
63 A. Sillen and Y. Engelborghs, *Photochem. Photobiol.*, 1998, **67**, 475.
64 C. Ullrich, *Time-Dependent Density-Functional Theory: Concepts and Applications*, Oxford University Press, 2012.
65 T. Yanai, D. P. Tew and N. C. Handy, *Chem. Phys. Lett.*, 2004, **393**, 51.
66 F. Weigend and R. Ahlrichs, *Phys. Chem. Chem. Phys.*, 2005, **7**, 3297.
67 S. Grimme, J. Antony, S. Ehrlich and H. Krieg, *J. Chem. Phys.*, 2010, **132**, 154104.
68 S. Grimme, S. Ehrlich and L. Goerigk, *J. Comput. Chem.*, 2011, **32**, 1456.
69 D. Andrae, U. Häußermann, M. Dolg, H. Stoll and H. Preuß, *Theor. Chim. Acta*, 1990, **77**, 123.
70 S. G. Balasubramani, P. G. Chen, S. Coriani, M. Diedenhofen, M. S. Frank, Y. J. Franzke, F. Furche, R. Grotjahn, M. E. Harding, C. Hättig, A. Hellweg, B. Helmich-Paris, C. Holzer, U. Huniar, M. Kaupp, A. Marefat Khah, S. Karbalaei Khani, T. Müller, F. Mack, B. D. Nguyen, S. M. Parker, E. Perlt, D. Rappoport, K. Reiter, S. Roy, M. Rückert, G. Schmitz, M. Sierka, E. Tapavicza, D. P. Tew, C. van Wüllen, V. K. Voora, F. Weigend, A. Wodyński and J. M. Yu, TURBOMOLE: Modular program suite for ab initio quantum-chemical and condensed-matter simulations, *J. Chem. Phys.*, 2020, **152**, 184107.
71 TURBOMOLE V7.6 2022, a development of University of Karlsruhe and Forschungszentrum Karlsruhe GmbH, 1989–2007, TURBOMOLE GmbH, since 2007; available from **https://www.turbomole.com**.
72 E. van Lenthe, E. J. Baerends and J. G. Snijders, *J. Chem. Phys.*, 1993, **99**, 4597.
73 E. van Lenthe, E. J. Baerends and J. G. Snijders, *Chem. Phys.*, 1994, **101**, 9783.
74 J. D. Rolfes, F. Neese and D. A. Pantazis, *J. Comput. Chem.*, 2020, **41**, 1842.
75 F. Neese, *Wiley Interdiscip. Rev.: Comput. Mol. Sci.*, 2012, **2**, 73.
76 F. Neese, *Wiley Interdiscip. Rev.: Comput. Mol. Sci.*, 2022, **12**, e1606.
77 F. Neese, F. Wennmohs, U. Becker and C. Riplinger, *J. Chem. Phys.*, 2020, **152**, 224108.
78 F. Weigend, *Phys. Chem. Chem. Phys.*, 2006, **8**, 1057.
79 F. Neese, *J. Chem. Phys.*, 2005, **122**, 034107.